



Article

# One-Pot Spray Engineering to Design $\text{Na}_{0.44}\text{MnO}_2$ Cathode Electrodes for High-Rate and Cycle-Stable Na-Ion Batteries

Bon-Ryul Koo <sup>1</sup>, Young-Geun Lee <sup>2</sup>, Sang Ho Lee <sup>3</sup>, Geon-Hyoung An <sup>2,4,\*</sup> and Chun Huang <sup>5,6,7,\*</sup>

- <sup>1</sup> Department of Materials, University of Oxford, Parks Road, Oxford OX1 3PH, UK  
<sup>2</sup> Department of Energy Engineering, Future Convergence Technology Research Institute, Gyeongsang National University, 33 Dongjin-ro, Jinju 52828, Gyeongnam, Korea  
<sup>3</sup> Department of Chemical Engineering, Pukyong National University, Busan 48513, Korea  
<sup>4</sup> Department of Energy System Engineering, Gyeongsang National University, 33 Dongjin-ro, Jinju 52828, Gyeongnam, Korea  
<sup>5</sup> Department of Materials, Imperial College London, London SW7 2AZ, UK  
<sup>6</sup> The Faraday Institution, Quad One, Becquerel Ave., Harwell Campus, Didcot OX11 0RA, UK  
<sup>7</sup> Research Complex at Harwell, Rutherford Appleton Laboratory, Didcot OX11 0FA, UK  
\* Correspondence: ghan@gntech.ac.kr (G.-H.A.); a.huang@imperial.ac.uk (C.H.)

**Abstract:** To improve the practical performance of Na-ion batteries, electrode structure engineering provides a new route to improve the electrochemical efficiency of the cathode active material. In this study, we suggest a new route of one-pot spray engineering to design  $\text{Na}_{0.44}\text{MnO}_2$  cathodes to realize high-rate and cycle-stable Na-ion battery performance. This technique adjusts the electrode structure from a dense to an open sponge-like morphology during layer-by-layer deposition of the materials. The sponge-like cathode results in improved ion insertion and transport kinetics, thus accelerating the rate capability with increased capacity and high-rate cycling capability (100.1 mAh/g and 90.2% cycling retention after 100 cycles at 5 C). These results highlight the potential for design engineering of cathode structures to achieve high-rate and cycle-stable performance for Na-ion batteries.

**Keywords:** sodium-ion battery; electrode structure;  $\text{Na}_{0.44}\text{MnO}_2$ ; one-pot spraying construction; open-pores networking structure



**Citation:** Koo, B.-R.; Lee, Y.-G.; Lee, S.H.; An, G.-H.; Huang, C. One-Pot Spray Engineering to Design  $\text{Na}_{0.44}\text{MnO}_2$  Cathode Electrodes for High-Rate and Cycle-Stable Na-Ion Batteries. *Batteries* **2022**, *8*, 181. <https://doi.org/10.3390/batteries8100181>

Academic Editor: Sylvain Franger

Received: 6 September 2022

Accepted: 10 October 2022

Published: 14 October 2022

**Publisher's Note:** MDPI stays neutral with regard to jurisdictional claims in published maps and institutional affiliations.



**Copyright:** © 2022 by the authors. Licensee MDPI, Basel, Switzerland. This article is an open access article distributed under the terms and conditions of the Creative Commons Attribution (CC BY) license (<https://creativecommons.org/licenses/by/4.0/>).

## 1. Introduction

As the use of renewable energy sources throughout the world increases to address net zero challenges, there is a rapidly increasing interest in battery applications that can store the intermittent electricity generated by these renewable sources. Lithium-ion batteries (LIBs) are the current widely used energy storage systems in applications ranging from portable electronic devices such as mobile phones, laptops, and cameras to large-scale devices such as electric vehicles and large-scale energy storage systems [1,2]. This accelerates the demand for lithium sources, which has caused its price to rise and threatened the possibility of its resource depletion [3]. The competition to develop easy-accessible, low-cost, and high-efficiency alternatives to the ubiquitous LIBs is progressing worldwide. Among these, sodium-ion batteries (SIBs) have received growing attention, which has resulted from the reserves of abundant sodium resources (2.83 wt%) compared to lithium (0.01 wt%) in the Earth's crust with reaction mechanisms and processing procedures similar to those of LIBs. In addition, sodium does not alloy with aluminum, and therefore aluminum foil can be used as the current collector for both the cathode and anode, which may replace the use of the more expensive and heavier copper as the current collector and is beneficial for realizing low-cost and large-scale applications with high gravimetric energy density. However, the larger ionic radius of sodium ions (1.02 Å) compared to lithium ions (0.76 Å) can negatively affect phase stability, transport properties, and interphase formation resulting in degradation of rate capability and cycling stability. The higher standard electrode potential of SIBs (−2.71 V vs. SHE in comparison with

−3.02 V vs. SHE for Li) also leads to reduced energy densities [4]. Therefore, the effort to improve the performance of SIBs based on an understanding of the electrochemical behavior of active materials and electrode structures should be explored [5].

In SIBs, cathodes have an important factor to determine their performance such as energy density and cycling life due to the relatively low specific capacity (100–200 mAh/g) compared to anodes (e.g., 250 mAh/g for hard carbon) [6–10]. There are challenges for successful cathode materials of SIBs to catch up with LIBs, including (1) ability to host a large number of Na ions; (2) high redox potential; (3) stable structural integrity during cycling; (4) large diffusion coefficient for Na ions and high electronic conductivity; (5) high chemical and thermal stabilities and compatibility with electrolytes; and (6) environmental friendliness and cost-effectiveness [11,12]. Among the pioneering developments of cathode materials of Na transition material oxide compounds ( $\text{Na}_x\text{M}_y\text{O}_z$ , M = Mn, Co, Ni, etc.), olivine phosphates, fluorophosphates, and Prussian blue analogs, [13–18], Na-Mn-O compounds have received an intensive attention for potential use in large-scale applications due to their high capacity, nontoxicity, and low cost [19]. The Na-Mn-O compounds can be classified into two kinds with layered and tunneled structures. For the layered structure ( $\text{NaMnO}_2$  and  $\text{Na}_{0.66}\text{MnO}_2$ ), it provides high specific capacity but limited cycling stability, whereas the tunneled structure exhibits good cycling stability but low specific capacity [20]. In addition, tremendous efforts have been tried for accelerating their performance through other research strategies, such as nanostructuring (e.g., nanorods [21], nanoplates [22]), surface modification (e.g., adding carbon or metal oxide layer [23]), and the introduction of multiple transition metals (e.g., Ni, Fe, and Ti [24–27]) to reduce electrical resistance, shorten Na ion diffusion paths, and improve interfacial comparability between electrode materials and electrolytes. However, although such extensive research of high-performance cathode materials delivers a hopeful message to raise the application possibilities of the SIBs, the mechanical and electrical failure relating to electrode-structural integrity is still an important issue that needs to be solved for the future battery industry.

High-rate cycling capability is an important factor for SIBs toward their applicability to practical products and a stepping stone for the development of the future battery industry [28,29]. During the charge and discharge process, unavoidable agglomeration and volume expansion of electrode materials and solid electrolyte interface (SEI) formation across the electrodes, trigger degradation mechanisms on the SIB performance. The uneven distribution of active materials restricts electron and ion diffusion due to carrier trapping centers formed from electrode-structural distortion, followed by electrode destruction at a larger scale with fractures, inducing extra SEI formation and detachment of the electrode from current collectors, resulting in inferior rate performance and poor cycling retention [30,31]. Modeling has provided important evidence of inherent problems at the electrode level that can threaten stability and battery performance due to partially applied overvoltage induced by the inhomogeneous occupation of Li ions and can suggest that these problems are also present in the electrodes of SIBs. The countermeasures used in LIBs include growing nano-arrayed architectures using  $\text{Co}_3\text{O}_4$  on current collectors with void gaps for buffering structural variations [32] and fabricating hybrid structures possessing an oriented face-to-face arrangement of Si and graphene that features robust structural stability [33]. Unfortunately, these approaches rely on exquisite and complex manufacturing techniques that could limit industrial battery applications. As an example of breakthroughs, our group has reported novel strategies of electrode engineering to design unique structures of layer-by-layer electrodes with different fractions of conductive additive and directional porosity with low tortuosity using scalable spray printing and freeze-casting methods, beneficial to battery performance [34–41]. Although electrode design is a key factor in effectively facilitating ion mobility, the gap between the performance of active materials themselves and the performance relating to electrode structures remains unresolved.

Herein, one-pot spray engineering of a new design of  $\text{Na}_{0.44}\text{MnO}_2$  cathode structure is investigated as a potential route to high-rate and cycle-stable SIBs. The adjustable design of the electrode from a dense to an open sponge-like structure is performed by

different concentrations of component solution during the one-pot spraying, which has been attributed to the direct layer-by-layer deposition of aggregations with size discrepancy and can effectively enhance the electrochemical kinetics and capacity for SIBs. In this study, the SIB with the open sponge-like electrode is noted to exhibit improved rate capacity compared to the dense one. The improved electrochemical performance is attributed to the unique effect of the open sponge-like structure to provide efficient and stable charge transportation within the electrode structure with short diffusion pathways and an improved specific surface area for Na ion interaction.

## 2. Experimental

For obtaining the  $\text{Na}_{0.44}\text{MnO}_2$  active material through sol-gel method, manganese (II) acetate tetrahydrates ( $(\text{CH}_3\text{COO})_2\text{Mn} \cdot 4\text{H}_2\text{O}$ , 99.99%, Sigma, Welwyn Garden City, UK) and sodium nitrate ( $\text{NaNO}_3$ , 99.0%, Sigma) with 0.46:1 of Na:Mn molar ratio were dissolved into deionized (DI) water with 0.1 M citric acid ( $\text{HOC}(\text{COOH})(\text{CH}_2\text{COOH})_2$ , 99.5%, Sigma) acting as chelating agent. After stirring for 1 h, the transparent solution was dried at 100 °C for 12 h until all the solvent evaporated. The resultant solid precursors were ground and then heat-treated at 800 °C for 10 h to obtain  $\text{Na}_{0.44}\text{MnO}_2$ . The spray suspensions were prepared by dispersing  $\text{Na}_{0.44}\text{MnO}_2$ , carbon conductivity enhancer (Super P, MTI Corporation, US), polyvinylidene fluoride (PVDF,  $M_w = 534,000$ , Sigma) binder as a weight ratio of 80:10:10 into a 70:30 vol% bi-solvent mixture of acetone (99.5%, Sigma) and 1-Methyl-2-pyrrolidinone (NMP, 99.5%, Sigma) by ultrasonic treatment for 30 min. The concentration of spray suspensions was adjusted to be 0.5, 4.0, 6.0, and 8.0 g/L to design the electrode from dense to porous structures. During the spray process, a copper foil or stainless steel disc was held on a vacuum chuck set heated to 150 °C. The suspensions were atomized by compressed air (~0.3 bar) through an industrial spray nozzle attached to an  $x$ - $y$ - $z$  linear manipulator gantry to directly deposit the suspension onto a controlled area on the current collector. Any solvent of the deposited suspension was instantly evaporated, resulting in the one-pot construction of the electrodes with different structures.

The morphology of the electrode structure was investigated using scanning electron microscopy (SEM) equipped with energy-dispersive X-ray spectroscopy (EDS) and a 3D surface confocal laser scanning microscope (3D surface CLSM, Carl Zeiss, Dresden, Germany). The machining of the electrode for cross viewing was carried out by a cross-section polisher (IB-09020CP, JEOL, Tokyo, Japan). The crystal structure was investigated using X-ray diffraction (XRD) with  $\text{Cu } K_\alpha$  radiation between 10 and 80° at a step size of 0.02°. The chemical composition and bonding states were analyzed by X-ray photoelectron spectroscopy (XPS, AXIS ultra-delay line detector equipped with an Al  $K_\alpha$  X-ray source, Korea Basic Science Institute, KBSI, Daedeok Headquarters). The wettability of the electrode in the electrolyte was investigated using a contact angle measurement system.

The profiling of electrochemical performance was performed within coin-type half cells assembled in an Ar-filled glovebox ( $\text{H}_2\text{O} < 0.1 \text{ ppm}$ ,  $\text{O}_2 < 0.1 \text{ ppm}$ ) with the prepared electrode as the cathode, a Na metal foil as the anode, a glass microfiber filter (GF/F, Whatman) as the separator, and a 1.0 M  $\text{NaClO}_4$  solution in a 1:1 vol.% mixture of ethylene carbonate (EC) and propylene carbonate (PC) as the electrolyte. The loading and packing density of the  $\text{Na}_{0.44}\text{MnO}_2$  electrodes were obtained by comparing the weight and thickness before and after the deposited layer. Galvanostatic charging/discharging was performed between 1.5 and 4.3 V at different current conditions (1 C-rate = 120 mA/g), rate capability was investigated at varying C-rates of 0.1, 0.2, 0.5, 1, 2, and 5 C, and the cycling retention was analyzed up to 100 cycles at a high 5 C-rate, all using an Arbin cycler system (Arbin BT-G-25) at room temperature. Cyclic voltammetry was performed at a range of scan rates of 0.1, 0.5, and 1 mV/s and electrochemical impedance spectroscopy (EIS) for the fresh and cycled (100 cycles) electrodes was carried out with an amplitude of 5 mV in the frequency range from  $10^5$  to  $10^{-2}$  Hz, both using an Autolab system (Metrohm) at room temperature. The

energy density ( $E$ , Wh/kg) and power density ( $P$ , W/kg) are calculated using galvanostatic charging/discharging tests, as using the following Equations (1) and (2) [1,4]:

$$E = \frac{1}{m} \int_0^t V(t) \cdot I \cdot dt \quad (1)$$

$$P = \frac{E}{dt} \quad (2)$$

where  $m$  is the weight of active material,  $V$  is the discharging voltage,  $I$  is the current density, and  $dt$  is the total discharge time.

### 3. Results and Discussion

Figure 1a–d shows the different electrode surfaces by varying the solution concentrations during the one-pot spraying process. Using the 0.5 g/L solution concentration (Figure 1a), the construction of a dense electrode structure was observed. Increasing the solution concentration to 6.0 g/L forms a porous network surface with an increased average pore size from 12.5  $\mu\text{m}$  for 4.0 g/L (Figure 1b,i) to 23.7  $\mu\text{m}$  for 6.0 g/L (Figure 1c) due to the interconnected agglomerates of the  $\text{Na}_{0.44}\text{MnO}_2$  nanorods (see Figure S1a). Figure 1i shows that at the same mass loading, as the solution concentration increases from 0.5 to 6 g/L, the packing density decreases until it becomes stable at 6 g/L. For a series of cross-section SEM images (Figure 1e–h), increasing solution concentration for spraying shows that the 6.0 g/L electrode has the same thickness as the 8.0 g/L electrode, indicating that an open sponge-like structure was constructed by the extension of the pores between the interconnected solid framework in the overall area from the surface into the current collector. For 8 g/L and above electrodes, the uneven structure is formed by the deposition of irregular agglomerates following the decrease of the measured thickness and pore size on the electrode structure, which does not have the benefit of an open sponge-like structure for the electrochemical reactions. There is no critical variation of the crystal structure of the  $\text{Na}_{0.44}\text{MnO}_2$  active material among the electrodes fabricated using the different solution concentrations, as indicated by emitted diffraction peaks of (130), (140), (200), and (360) at 13.96, 16.68, and 19.45, and 35.92°, respectively, indicating the orthorhombic structure with  $Pbam$  space group (JCPDS No. 27-0750) (Figure 1j) and the balanced intensity ratio of  $\text{Mn}^{3+}/\text{Mn}^{4+}$  (intensity ratio 1) calculated from the Mn 2p spectra (see Figure S1b) [42,43].

The mechanism of the  $\text{Na}_{0.44}\text{MnO}_2$  electrode structure adjustment from dense to open sponge-like structures by one-pot spraying can be attributed to the stacking behavior of the solid component during layer-by-layer deposition of the suspension. During spraying (Figure 2a), the spray nozzle atomizes the suspension into numerous micro-droplets which tend to form aggregations as a result of drying in the vicinity of the heated substrate [25]. The concentration of the suspension is a major factor in determining the degree of aggregate, affecting the resultant aggregation size [44]. For low-concentration suspensions, the solid components induced from spread droplets were stacked up one by one neatly, resulting in a dense electrode structure by filling the sprayed components in the empty space by the layer-by-layer deposition, as confirmed by the SEM images of the electrodes with increasing mass loadings using the same suspension concentration of 0.5 g/L (Figure S2a–c). The fully filled body (EDS mapping of Mn element in the cross-section of the 0.5 g/L electrode, see Figure 2b) and smooth surface (line profile of 3D surface CLSM, Figure 2c,d) were clearly observed in the electrode structure. On the other hand, a high concentration suspension could limit the spreading of the droplets, leading to the enlargement of the resultant aggregation sizes (EDS mapping of Mn element in the cross-section of the 6.0 g/L electrode, see Figure 2e). Hence, during the gradual stacking of the solid component on the current collector (Figure S2d–f), the enlarged aggregations lead to the formation of the vacant areas between them from the bottom to the top of the electrode (see Figure 2e) due to the heterogeneous interlocking of the deposited product (Figure 2f,g), leading to the construction of free pathway networks for electrolyte penetration and an adequate

surface area to accommodate violent structural deformation of the electrode induced by the electrochemical reactions of the Na ions [45].

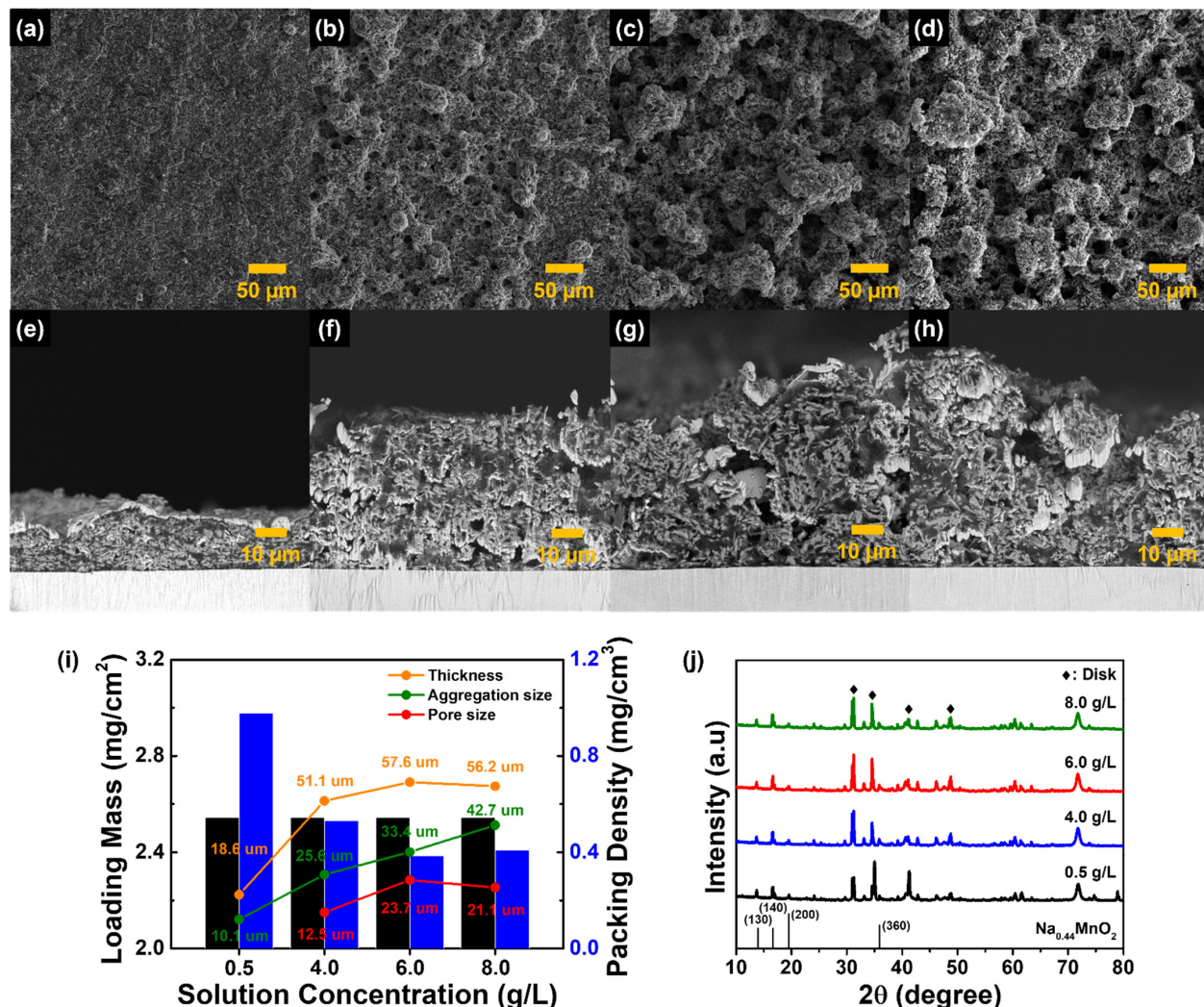


**Figure 1.** (a–d) Surface-view and (e–h) cross-section SEM images of the Na<sub>0.44</sub>MnO<sub>2</sub> electrodes with increasing solution concentrations from 0.5 to 8.0 g/L fabricated by the one-pot spraying process, (i) comparison of the electrode factors (loading mass (black histogram), packing density (blue histogram), thickness, aggregation size, and pore size) with the varying solution concentrations, and (j) the XRD curves of all the electrodes.

The galvanostatic charge/discharge voltage profiles measured at 0.1 C expose a difference in the electrochemical behavior among the electrodes (Figure 3a). Compared to the dense electrode structure made by the suspension concentration of 0.5 g/L, the charge/discharge profiles of the electrodes made by the higher suspension concentrations show six more distinct plateaus, indicating the consecutive phase transitions of Na<sub>0.44</sub>MnO<sub>2</sub> during Na-ion intercalation and deintercalation [46], especially for the electrode made by the suspension concentration of 6.0 g/L, resulting in the maximum of the initial discharge capacity (121.6 mAh/g). This is attributed to the open channels within the electrode providing an effective surface area for the electrochemical reactions of the Na ions with the Na<sub>0.44</sub>MnO<sub>2</sub> active material [32]. Furthermore, as shown in Figure 3b,d, while the 0.5 g/L electrode shows rapid degradation of the specific capacity at the accelerated current densities from 0.1 to 10 C, the 6.0 g/L electrode exhibited superior capacity value and capacity retention at increasing C rates to 10 C. The 6.0 g/L electrode also exhibited higher volumetric capacities at 1 C and higher rates (Figure 3c), which can be attributed to the improved

anodic diffusion coefficient of the Na ion ( $D$ ,  $\text{cm}^2/\text{s}$ , Figure 3e) that is derived by a linear relation based on peak current ( $I_p$ , mA) and scan rate ( $v$ ) based on the Randles–Sevcik equation (Equation (3)) from the cyclic voltammograms in Figure S4, as follows: [47,48]

$$\frac{I_p}{m} = 0.4463 \left( \frac{F}{RT} \right)^{1/2} AD^{1/2} C v^{1/2} \quad (3)$$

where  $m$  is the electrode mass,  $F$  is the Faraday constant (96,486 C/mol),  $R$  is the gas constant (8.314 J/mol K),  $T$  is the temperature,  $A$  is the electrode area per unit mass (in  $\text{cm}^2/\text{g}$ ), and  $C$  is the Na-ion concentration of the electrodes. The  $D$  values of the charging and discharging processes increased from the 0.5 g/L electrode to the 6.0 g/L electrode and then descended for the 8.0 g/L electrode (see Figure 3e and Table S1), which indicates that the open sponge-like structures tend to promote efficient delivery of Na ions to the  $\text{Na}_{0.44}\text{MnO}_2$  active materials. In addition, the 6.0 g/L electrode (117.0  $\Omega$ ) showed a decreased charge transfer resistance ( $R_{ct}$ ) as reflected from the smaller semicircle in the high medium-frequency region in the electrochemical impedance spectroscopy (EIS) spectra (see Figure 3f) when compared to the other electrodes (564.0  $\Omega$  for the 0.5 g/L electrode, 301.5  $\Omega$  for the 4.0 g/L electrode, and 222.3  $\Omega$  for the 8.0 g/L and 390.3–1000.22  $\Omega$  in the literature for slurry coated electrodes [49–51]), which also indicates excellent charge transfer ability for the open sponge-like structures. This can prove to relax resistance for transporting both Na ions and electrons within the electrode [52]. Figure 3g,h shows that the 6.0 g/L electrode exhibited the highest gravimetric energy and power densities at all C rates and the highest volumetric energy and power densities above 1 C, demonstrating its benefits, particularly at faster C rates.

Figure 4a shows the superior cycling capability of the 6.0 g/L cathode compared with the 0.5 g/L electrode at 0.1 C for 10 cycles and then at a high rate of 5 C for 90 cycles. After 100 cycles, the 6.0 g/L electrode maintained a specific capacity value of 100.1 mAh/g (90.2% cycling retention) despite the high C-rate (5 C), whereas the capacity of the 0.5 g/L electrode considerably degraded to 32.5 mAh/g (34% cycling retention). The corresponding volumetric capacities are shown in Figure S3, showing doubling volumetric capacity for the 6.0 g/L cathode at 5 C after 100 cycles. The stable high-rate electrochemical behavior of the 6.0 g/L electrode is attributed to the unique structure that provides an efficient pathway to access and accept abundant Na ions in the high-rate electrochemical reactions [46]. This corroborates the excellent electrochemical kinetic properties shown by the highest Na-ion diffusion coefficient  $D$  and lowest  $R_{ct}$  of the EIS spectra (see Figure 3e). In order to further investigate the unique effect of the open-pores networking structure on Na storage behavior at the electrochemical reaction, we carried out the calculation of the degree of capacitive effect of the electrodes via the relationship between measured current ( $i$ ) and scan rate ( $v$ ) of the CV curves ( $i = av^b$ , where  $a$  and  $b$  are constants) [53,54]. In Figure 4b, the gradient of the log  $i$ –log  $v$  plot deducts the  $b$  value depending on the applied voltage to indicate the proportion of capacitance-controlled behavior, as shown in the detailed value in Figure S5. The  $b$  value determined from the gradient of the log  $i$ –log  $v$  plot is in the range between 0.5 and 1.0, where  $b = 0.5$  indicates a diffusion-controlled behavior and  $b = 1$  indicates a capacitance-controlled process. That is, the larger the  $b$  value, the greater the contribution of the faster surface redox reaction during charging/discharging [55]. It is noted that the  $b$  values of the 6.0 g/L electrode at the specific voltages generating the electrochemical reactions between the Na ions and electron electrode are higher than those of the 0.5 g/L electrode, which can mean generating more profound capacitive kinetics for the Na storage [56]. In the CV curve of the 6.0 g/L electrode at 0.5 mV/s (Figure 4c), there are six main pairs of redox peaks indicating the charge ordering during the electrochemical behavior of the  $\text{Na}_{0.44}\text{MnO}_2$  electrodes [5,11] (the other CV curves for both 0.5 g/L and 6.0 g/L electrodes at various scan rates ( $v$ ) of 0.1, 0.5, and 1 mV/s are shown in Figure S4). We also obtained the quantification of ion diffusion and surface induced capacitance contributions for each of the peaks from the CV curve. It revealed two parts of the surface

induced capacitive ( $k_1\nu$ ) and ion diffusion-controlled intercalation ( $k_2\nu^{1/2}$ ) contributions for each of the peaks by using the following equation (Equation (4)) [57,58]:

$$i(V) = k_1\nu + k_2\nu^{1/2} \quad (4)$$

or

$$i(V)/\nu^{1/2} = k_1/\nu^{1/2} + k_2 \quad (5)$$

Equation (5) means that  $k_1$  and  $k_2$  can be obtained from the slope and intercept, respectively, of a linear plot of  $i(V)/\nu^{1/2}$  versus  $\nu^{1/2}$ <sup>55</sup>. The plot (Figure 4d) for the qualitative comparison between the electrodes shows that the capacitive contribution is gradually improved with increasing the scan rate, which is attributed to the capacitive mechanism based on insertion/extraction of Na ions as a main factor affecting the electrochemical reactions of the electrodes [59]. Interestingly, the capacitive contribution of the 6.0 g/L electrode is higher than that of the 0.5 g/L electrode at overall scan rates. This indicates that the efficient charge transportation via the open-pores networking electrode structure activates the short diffusion pathway and improves the specific surface area of the composite  $\text{Na}_{0.44}\text{MnO}_2$  active materials, which is attributed to the improved wettability of the porous structure with the electrolytes, as confirmed by the wettability test where the contact angle is reduced from 112.3 to 60.3° (Figure 4e,f).

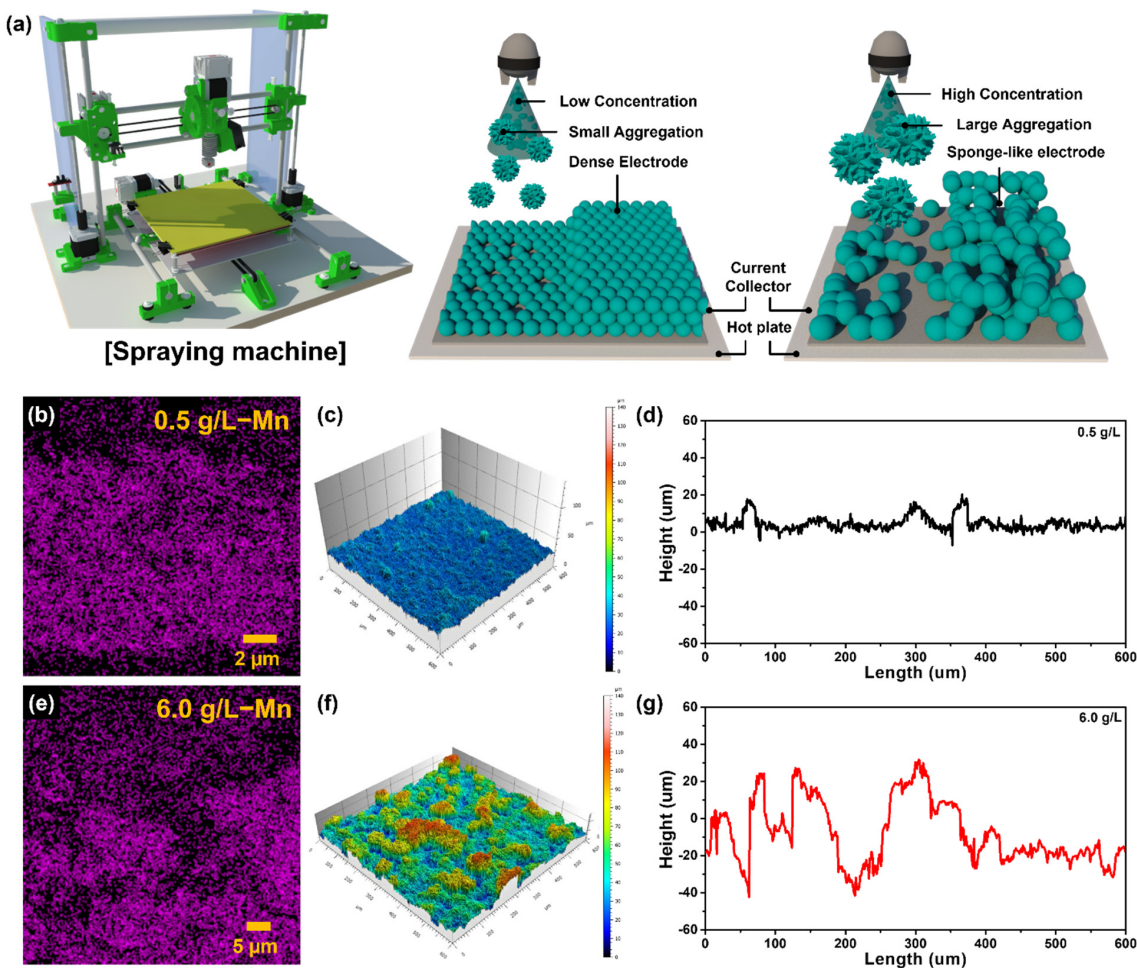


**Figure 2.** (a) Schematic mechanism of controllable engineering the  $\text{Na}_{0.44}\text{MnO}_2$  electrode structure using different suspension concentrations during the one-pot spraying process, the EDS images of Mn element to visualize the cross section of electrode structures ((b) 0.5 g/L electrode and (e) 6.0 g/L electrode), and the 3D surface images and the resultant height plots of (c,d) 0.5 g/L electrode and (f,g) 6.0 g/L electrode using 3D surface confocal laser scanning microscope.

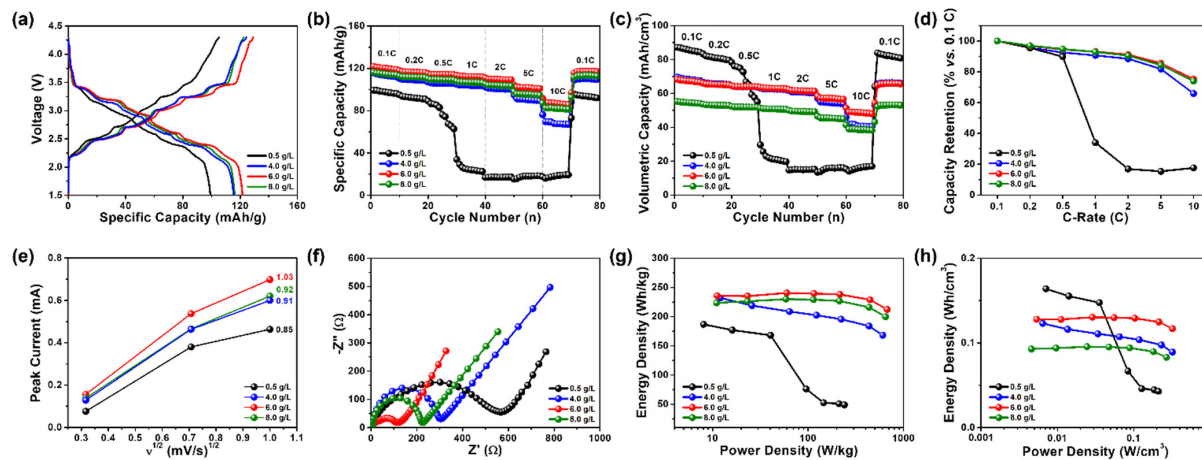


**Figure 3.** (a) The galvanostatic charge/discharge voltage profiles measured in range of 1.5–4.3 V at 0.1 C, (b) rate capability in (b) specific and (c) volumetric capacities, (d) plot of capacity retention in increased C-rate conditions, (e) relationship of peak current density with respect to the varied scan rates for the electrodes made by 0.5 g/L and 6.0 g/L suspension concentrations during cathodic and anodic reactions, (f) EIS spectra and curves showing the energy and power densities of the SIB cells in (g) the specific and (h) volumetric conditions.

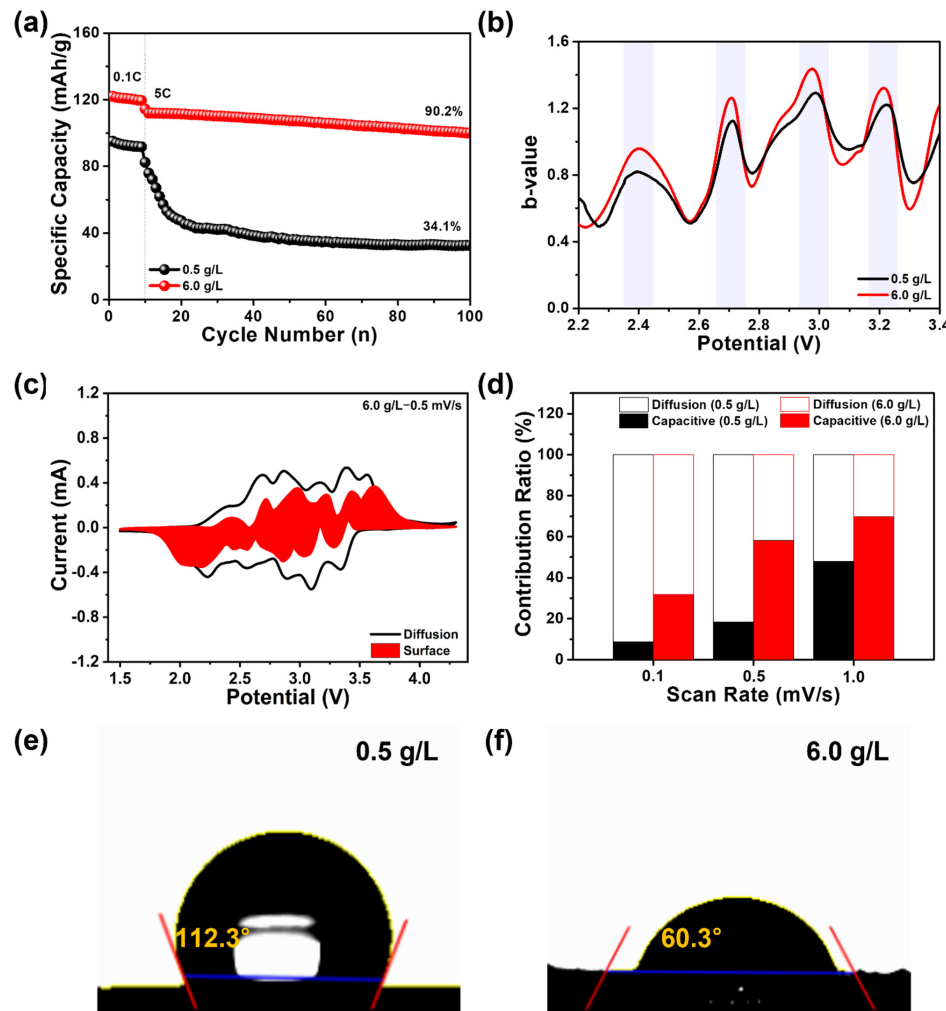


**Figure 4.** (a) high-rate cycling capability; (b) continuous b-value measured in potential range from 2.2 to 3.4 V along the cathodic scan; (c) CV curves of the 6.0 g/L electrode at 0.5 mV/s; each characteristic

peak has the ion diffusion and surface induced capacitance contributions; (d) the quantification of ion diffusion and surface induced capacitance of the electrodes from the CV curves; and the visual results of wetting angle between the electrolyte and electrode surface; ((e) 0.5 g/L electrode; and (f) 6.0 g/L electrode).

To better understand the design role of the  $\text{Na}_{0.44}\text{MnO}_2$  electrode structure on the high-rate cycling capability of the SIBs, ex situ XRD was used to trace the electrochemical behavior of the Na ions after cycling from the lattice [60,61]. In Figure 5a, the patterns of the 0.5 g/L electrode after 100 cycles between 1.5 and 4.3 V at the 5 C-rate show a shift of the diffraction peaks toward larger  $2\theta$  values from 1.5 to 4.3 V [62]. There was a larger peak shift for the 6.0 g/L electrode (Figure 5b) than the 0.5 g/L electrode. This is in agreement with the Mn 2p XPS result showing peaks relating to the Mn ions for the 6.0 g/L electrode, whereas the Mn 2p spectrum of the 0.5 g/L electrode does not show obvious peaks due to excessive emergence of irreversible Na-related compounds (Figure S6). The reversible processes in the crystal structure (see ex situ XRD) and chemical bonds (see XPS) are expected to follow the soft movement of sodium ions and electrons. That is, the observed difference in the electrochemical behavior can be linked to the internal resistance of the electrodes. The EIS plot in Figure 5c,d shows that  $R_{ct}$  increased much more significantly for the 0.5 g/L electrode and at a faster C rate compared with the 6.0 g/L electrode, indicating increasing internal resistance during the extraction/insertion of the Na ions, resulting in obsolete cycling capacity due to the serious deformation of the electrode structure induced by component condensation, as shown in the SEM images of the post-mortem electrodes in Figure 5e,f [63]. In contrast, the SEM images in Figure 5g,h show that the structure of the 6.0 g/L electrode is maintained, ensuring the realization of superb high-rate and cycle-stable capabilities for SIBs.

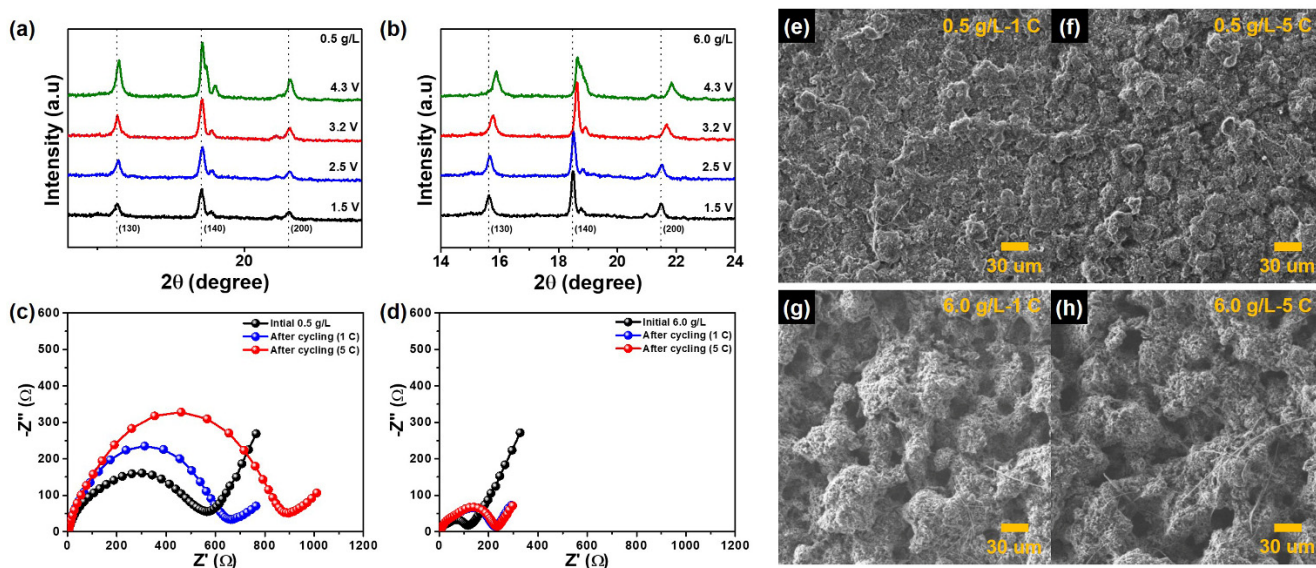


**Figure 5.** Ex situ XRD results of (a) 0.5 g/L electrode and (b) 6.0 g/L electrode, EIS Nyquist plot after 100 cycles at 1 and 5 C-rate for (c) 0.5 g/L electrode and (d) 6.0 g/L electrode, and the resultant SEM images after high-rate cycling measurement (e,g) 0.5 g/L electrode and (f,h) 6.0 g/L electrode).

#### 4. Conclusions

A cathode material of  $\text{Na}_{0.44}\text{MnO}_2$  was synthesized, and a unique open sponge-like cathode structure was fabricated via controlled engineering of a one-pot spraying process for Na-ion batteries. The one-pot spraying process directly adjusts the electrode structures from dense to porous by adjusting the spraying suspension concentration. The critical suspension concentration (6.0 g/L) drives the direct layer-by-layer deposition of enlarged aggregations on the substrate to make the electrode structure with the vacant areas ranging from bottom to top. As a result, the open sponge-like electrode structure

realizes higher specific capacity, rate capability, and capacity retention compared to the dense electrode (0.5 g/L), which can be induced by the improved diffusion coefficient and enriched electroactive sites in the electrochemical reactions of the Na ions with the electrode interfaces. In addition, the high-rate cycling capability of the open sponge-like electrode is noted in both the specific (100.1 mAh/g and 90.2% cycling retention after 100 cycles at 5 C). The superior electrochemical performance is attributed to the efficient and stable charge transportation via the open-pores networking electrode structure for providing the shortened diffusion pathway and improved specific surface area to the composite  $\text{Na}_{0.44}\text{MnO}_2$  electrode. The  $\text{Na}_{0.44}\text{MnO}_2$  active material exhibits reversible phase transition during the high-rate electrochemical reaction with Na ions as shown in the ex situ XRD. Additionally, the electrode structure is maintained over cycling as a result of maintaining the low internal resistance of the electrodes in the condition of increasing C-rate. To the best of the present authors' knowledge, this is the first report on the unique design of the cathode electrodes with superior high-rate capabilities of the SIBs through the one-pot spraying process, and we believe that one-pot spray engineering can be utilized as a potential milestone to boost the development of advanced structures for high-rate and cycle-stable SIBs.

**Supplementary Materials:** The following supporting information can be downloaded at: <https://www.mdpi.com/article/10.3390/batteries8100181/s1>.

**Author Contributions:** Conceptualization, C.H. and B.-R.K.; data curation, G.-H.A.; formal analysis, B.-R.K.; project administration, C.H.; resources, C.H.; supervision, C.H.; validation, S.H.L.; visualization, Y.-G.L.; writing—original draft, B.-R.K.; writing—review and editing, C.H. and G.-H.A. All authors have read and agreed to the published version of the manuscript.

**Funding:** This research was supported by the Engineering and Physical Sciences Research Council (EPSRC) UKRI Innovation Fellowship (EP/S001239/1, EP/S001239/2), the Faraday Industry Fellowship (FIIF015), the Faraday Institution Training Grant (FITG034), and the Imperial College London UKRI Impact Acceleration Account (EP/X52556X/1).

**Conflicts of Interest:** The authors declare no conflict of interest.

## References

- Huang, C.; Leung, C.L.A.; Leung, P.; Grant, P.S. A solid-state battery cathode with a polymer composite electrolyte and low tortuosity microstructure by directional freezing and polymerization. *Adv. Energy Mater.* **2021**, *11*, 2002387. [[CrossRef](#)]
- Yang, S.; Zhang, F.; Ding, H.; He, P.; Zhou, H. Lithium metal extraction from seawater. *Joule* **2018**, *2*, 1648. [[CrossRef](#)]
- Liu, Q.; Hu, Z.; Chen, M.; Zou, C.; Jin, H.; Wang, S.; Chou, S.-L.; Liu, Y.; Dou, S.-X. The cathode choice for commercialization of sodium-ion batteries: Layered transition metal oxides versus prussian blue analogs. *Adv. Funct. Mater.* **2020**, *30*, 1909530. [[CrossRef](#)]
- Hwang, J.Y.; Myung, S.T.; Sun, Y.K. Sodium-ion batteries: Present and future. *Chem. Soc. Rev.* **2017**, *46*, 3529. [[CrossRef](#)] [[PubMed](#)]
- Chandra, M.; Shukla, R.; Rashid, M.; Gupta, A.; Basu, S.; Dhaka, R.S. Synthesis and physical properties of  $\text{Na}_x\text{TO}_2$  ( $T = \text{Mn}, \text{Co}$ ) nanostructures for cathode materials in Na-ion batteries. *Mater. Res. Bull.* **2018**, *105*, 178. [[CrossRef](#)]
- Xiang, X.; Zhang, K.; Chen, J. Recent advances and prospects of cathode materials for sodium-ion batteries. *Adv. Mater.* **2015**, *27*, 5343. [[CrossRef](#)]
- Golubkov, A.W.; Fuchs, D.; Wagner, J.; Wiltsche, H.; Stangl, C.; Fauler, G.; Voitic, G.; Thaler, A.; Hacker, V. Thermal-runaway experiments on consumer Li-ion batteries with metal-oxide and olivin-type cathodes. *RCS Adv.* **2014**, *4*, 3633. [[CrossRef](#)]
- Xiao, B.; Soto, F.A.; Gu, M.; Han, K.S.; Song, J.; Wang, H.; Engelhard, M.H.; Murugesan, V.; Mueller, K.T.; Reed, D.; et al. Lithium-pretreated hard carbon as high-performance sodium-ion battery anodes. *Adv. Energy Mater.* **2018**, *8*, 1801441. [[CrossRef](#)]
- Wu, J.; Liu, J.; Cui, J.; Yao, S.; Ihsan-UI-Haq, M.; Mubarak, N.; Quattrochi, E.; Ciucci, F.; Kim, J.-K. Dual-phase  $\text{MoS}_2$  as a high-performance sodium-ion battery anode. *J. Mater. Chem. A* **2020**, *8*, 2114. [[CrossRef](#)]
- Ran, L.; Luo, B.; Gentle, L.R.; Lin, T.; Sun, Q.; Li, M.; Rana, M.M.; Wang, L.; Knibbe, R. Biomimetic  $\text{Sn}_4\text{P}_3$  anchored on carbon nanotubes as an anode for high-performance sodium-ion batteries. *ACS Nano* **2020**, *14*, 8826. [[CrossRef](#)]
- Fang, Y.; Zhang, J.; Xiao, L.; Ai, X.; Cao, Y.; Yang, H. Phosphate framework electrode materials for sodium ion batteries. *Adv. Sci.* **2017**, *4*, 1600392. [[CrossRef](#)] [[PubMed](#)]
- Zhu, L.; Li, L.; Wen, J.; Zeng, Y.R. Structural stability and ionic transport property of  $\text{NaMPO}_4$  ( $M = \text{V}, \text{Cr}, \text{Mn}, \text{Fe}, \text{Co}, \text{Ni}$ ) as cathode material for Na-ion batteries. *J. Power Sources* **2019**, *438*, 227016. [[CrossRef](#)]
- Dacek, S.T.; Richards, W.D.; Kitchaev, D.A.; Ceder, G. Structure and dynamics of fluorophosphate Na-ion battery cathodes. *Chem. Mater.* **2016**, *28*, 5450. [[CrossRef](#)]

14. Chao, D.; Lai, C.-H.; Liang, P.; Wei, Q.; Wang, Y.-S.; Zhu, C.; Deng, G.; Doan-Nguyen, V.V.T.; Lin, J.; Mai, L.; et al. Sodium vanadium fluorophosphates (NVOPF) array cathode designed for high-rate full sodium ion storage device. *Adv. Energy Mater.* **2018**, *8*, 1800058. [[CrossRef](#)]
15. Wang, B.; Han, Y.; Wang, X.; Bahlawane, N.; Pan, H.; Yan, M.; Jiang, Y. Prussian blue analogs for rechargeable batteries. *iScience* **2018**, *3*, 110. [[CrossRef](#)]
16. Du, G.; Tao, M.; Li, J.; Yang, T.; Gao, W.; Deng, J.; Qi, Y.; Bao, S.J.; Xu, M. Low-operating temperature, high-rate and durable solid-state sodium-ion battery based on polymer electrolyte and prussian blue cathode. *Adv. Energy Mater.* **2020**, *10*, 1903351. [[CrossRef](#)]
17. Yoo, G.; Koo, B.-R.; An, H.-R.; Huang, C.; An, G.-H. Enhanced and stabilized charge transport boosting by Fe-doping effect of  $V_2O_5$  nanorod for rechargeable Zn-ion battery. *J. Ind. Eng. Chem.* **2021**, *99*, 344. [[CrossRef](#)]
18. Tapia-Ruiz, N.; Dose, W.M.; Sharma, N.; Chen, H.; Heath, J.; Somerville, J.W.; Maitra, U.; Islam, M.S.; Bruce, P.G. High voltage structural evolution and enhanced Na-ion diffusion in  $P_2\text{-Na}_{2/3}\text{Ni}_{1/3-x}\text{Mg}_x\text{Mn}_{2/3}\text{O}_2$  ( $0 \leq x \leq 0.2$ ) cathodes from diffraction, electrochemical and ab initio studies. *Energy Environ. Sci.* **2018**, *11*, 1470. [[CrossRef](#)]
19. Islam, M.S.; Fisher, C.A.J. Lithium and sodium battery cathode materials: Computational insights into voltage, diffusion and nanostructural properties. *Chem. Soc. Rev.* **2014**, *43*, 185. [[CrossRef](#)]
20. Ma, G.; Zhao, Y.; Huang, K.; Ju, Z.; Liu, C.; Hou, Y.; Xing, Z. Effects of the starting materials of  $\text{Na}_{0.44}\text{MnO}_2$  cathode materials on their electrochemical properties for Na-ion batteries. *Electrochim. Acta* **2016**, *222*, 36. [[CrossRef](#)]
21. He, X.; Wang, J.; Qiu, B.; Paillard, E.; Ma, C.; Cao, X.; Liu, H.; Stan, M.C.; Liu, H.; Gallash, T.; et al. Durable high-rate capability  $\text{Na}_{0.44}\text{MnO}_2$  cathode material for sodium-ion batteries. *Nano Energy* **2016**, *27*, 602. [[CrossRef](#)]
22. Zhang, J.; Yu, D.Y.W. Stabilizing  $\text{Na}_{0.7}\text{MnO}_2$  cathode for Na-ion battery via a single-step surface coating and doping process. *J. Power Sources* **2018**, *391*, 106. [[CrossRef](#)]
23. Wang, J.; Zhou, Q.; Liao, J.; Ding, X.; Hu, Q.; He, X.; Chen, C.-H. Suppressing the Unfavorable Surface Layer Growth on  $\text{Na}_{0.44}\text{MnO}_2$  Cathode by a  $\text{NaTi}_2(\text{PO}_4)_3$  Coating To Improve Cycling Stability and Ultrahigh Rate Capability. *ACS Appl. Energy Mater.* **2019**, *2*, 7497. [[CrossRef](#)]
24. Zhou, X.; Zhao, A.; Chen, Z.; Cao, Y. Research progress of tunnel-structural  $\text{Na}_{0.44}\text{MnO}_2$  cathode for sodium-ion batteries: A mini review. *Electrochem. Commun.* **2021**, *122*, 106897. [[CrossRef](#)]
25. Whitacre, J.F.; Tevar, A.; Sharma, S.  $\text{Na}_4\text{Mn}_9\text{O}_{18}$  as a positive electrode material for an aqueous electrolyte sodium-ion energy storage device. *Electrochem. Commun.* **2010**, *12*, 463. [[CrossRef](#)]
26. Doeff, M.M.; Richardson, T.J.; Hwang, K.-T. Electrochemical and structural characterization of titanium-substituted manganese oxides based on  $\text{Na}_{0.44}\text{MnO}_2$ . *J. Power Sources* **2004**, *135*, 240. [[CrossRef](#)]
27. Zhong, Y.; Yang, M.; Zhou, X.; Zhou, Z. Structural design for anodes of lithium-ion batteries: Emerging horizons from materials to electrodes. *Mater. Horiz.* **2015**, *2*, 553. [[CrossRef](#)]
28. Wu, J.; Yang, S.; Cai, W.; Bi, Z.; Shang, G.; Yao, J. Multi-characterization of  $\text{LiCoO}_2$  cathode films using advanced AFM-based techniques with high resolution. *Sci. Rep.* **2017**, *7*, 11164. [[CrossRef](#)]
29. Li, Y.; Tan, B.; Wu, Y. Mesoporous  $\text{Co}_3\text{O}_4$  nanowire arrays for lithium ion batteries with high capacity and rate capability. *Nano Lett.* **2008**, *8*, 265. [[CrossRef](#)]
30. Zhong, Y.; Yang, M.; Zhou, X.; Luo, Y.; Wei, J.; Zhou, Z. Orderly packed anodes for high-power lithium-ion batteries with super-long cycle life: Rational design of  $\text{MnCO}_3$ /Large-area graphene composites. *Adv. Mater.* **2015**, *27*, 806. [[CrossRef](#)]
31. Lee, S.H.; Huang, C.; Johnston, C.; Grant, P.S. Spray printing and optimization of anodes and cathodes for high performance Li-Ion batteries. *Electrochim. Acta* **2018**, *292*, 546. [[CrossRef](#)]
32. Huang, C.; Dontigny, M.; Zaghib, K.; Grant, P.S. Low-tortuosity cathodes by ice and graded lithium ion battery templating. *J. Mater. Chem. A* **2019**, *7*, 21421. [[CrossRef](#)]
33. Lee, S.H.; Huang, C.; Grant, P.S. Multi-layered composite electrodes of high power  $\text{Li}_4\text{Ti}_5\text{O}_{12}$  and high capacity  $\text{SnO}_2$  for smart lithium ion storage. *Energy Storage Mater.* **2021**, *38*, 70. [[CrossRef](#)]
34. Sung, K.-W.; Koo, B.-R.; Ahn, H.-J. Hybrid nanocomposites of tunneled-mesoporous sulfur-doped carbon nanofibers embedded with zinc sulfide nanoparticles for ultrafast lithium storage capability. *J. Alloys Compd.* **2021**, *854*, 157206. [[CrossRef](#)]
35. Lee, S.H.; Huang, C.; Grant, P.S. High energy lithium ion capacitors using hybrid cathodes comprising electrical double layer and intercalation host multi-layers. *Energy Storage Mater.* **2020**, *33*, 408. [[CrossRef](#)]
36. Lee, S.H.; Huang, C.; Grant, P.S. Layer-by-layer printing of multi-layered heterostructures using  $\text{Li}_4\text{Ti}_5\text{O}_{12}$  and Si for high power Li-ion storage. *Nano Energy* **2019**, *61*, 96. [[CrossRef](#)]
37. Huang, C.; Grant, P.S. Coral-like cathodes by ice directional porosity lithium ion battery templating. *J. Mat. Chem. A* **2018**, *6*, 14689. [[CrossRef](#)]
38. Huang, C.; Young, N.P.; Zhang, J.; Snaith, H.J.; Grant, P.S. A two layer electrode structure for improved Li Ion diffusion and volumetric capacity in Li Ion batteries. *Nano Energy* **2017**, *31*, 377. [[CrossRef](#)]
39. Xu, R.; Yang, Y.; Yin, F.; Liu, P.; Cloetens, P.; Liu, Y.; Lin, F.; Zhao, K.J. Heterogeneous damage in Li-ion batteries: Experimental analysis and theoretical modeling. *Mech. Phys. Solids* **2019**, *129*, 160. [[CrossRef](#)]
40. Shasien, M.; Suzuki, M.; Tsutai, Y. Controlling the coating microstructure on axial suspension plasma spray process. *Surf. Coat. Technol.* **2018**, *356*, 96.

41. Zhang, X.; Ju, Z.; Housel, L.M.; Wang, L.; Zhu, Y.; Singh, G.; Sadique, N.; Takeuchi, K.J.; Takeuchi, E.S.; Marschilok, A.C.; et al. Promoting transport kinetics in Li-ion battery with aligned porous electrode architectures. *Nano Lett.* **2019**, *19*, 8255. [[CrossRef](#)] [[PubMed](#)]
42. Shi, W.-J.; Yan, Y.-W.; Chi, C.; Ma, X.-T.; Zhang, D.; Xu, S.-D.; Chen, L.; Wang, X.-M.; Liu, S.-B. Fluorine anion doped  $\text{Na}_{0.44}\text{MnO}_2$  with layer-tunnel hybrid structure as advanced cathode for sodium ion batteries. *J. Power Sources* **2019**, *427*, 129. [[CrossRef](#)]
43. Zhong, W.; Huang, Q.; Zheng, F.; Deng, Q.; Pan, Q.; Liu, Y.; Li, Y.; Hu, J.; Yang, C.; Liu, M. Structural insight into the abnormal capacity of Co-substitution tunnel-type  $\text{Na}_{0.44}\text{MnO}_2$  cathode for sodium ion batteries. *ACS Appl. Mater. Interfaces* **2020**, *12*, 47548. [[CrossRef](#)] [[PubMed](#)]
44. Francia, V.; Martín, L.; Bayly, A.E.; Simmons, M.J.H. Particle aggregation in large counter-current spray drying towers: Nozzle configuration, vortex momentum and temperature. *Procedia Eng.* **2015**, *102*, 668. [[CrossRef](#)]
45. Jia, H.; Li, X.; Song, J.; Zhang, X.; Luo, L.; He, Y.; Li, B.; Cai, Y.; Hu, S.; Xiao, X.; et al. Hierarchical porous silicon structures with extraordinary mechanical strength as high performance lithium-ion battery anodes. *Nat. Commun.* **2020**, *11*, 1474. [[CrossRef](#)] [[PubMed](#)]
46. Koo, B.-R.; Ahn, H.-J. Fast-switching electrochromic properties of mesoporous  $\text{WO}_3$  films with oxygen vacancy defects. *Nanoscale* **2017**, *9*, 17788. [[CrossRef](#)]
47. Yang, Y.; Chen, D.; Lu, B.; Zhao, J. Binder-free Si nanoparticle electrode with 3D porous structure prepared by electrophoretic deposition for lithium-ion batteries. *J. ACS Appl. Mater. Interfaces* **2015**, *7*, 7497. [[CrossRef](#)]
48. Feng, F.; Chen, S.; Liao, X.-Z.; Ma, Z.-F. Hierarchical hollow prussian blue rods synthesized via self-sacrifice template as cathode for high performance sodium ion battery. *Small Methods* **2019**, *3*, 1800259. [[CrossRef](#)]
49. Liu, C.; Guo, W.-L.; Wang, Q.-H.; Li, J.-G.; Yang, X.-P. Parametric study of hydrothermal soft chemical synthesis and application of  $\text{Na}_{0.44}\text{MnO}_2$  nanorods for Li-ion battery cathode materials: Synthesis conditions and electrochemical performance. *J. Alloys Compd.* **2016**, *658*, 588. [[CrossRef](#)]
50. Xia, H.; Zhu, X.; Liu, J.; Liu, Q.; Lan, S.; Zhang, Q.; Liu, X.; Seo, J.K.; Chen, T.; Gu, L.; et al. Elucidating anionic oxygen activity in lithium-rich layered oxides. *Nat. Commun.* **2018**, *9*, 5100. [[CrossRef](#)]
51. Shen, Q.; Zhao, X.; Liu, Y.; Li, Y.; Zhang, J.; Zhang, N.; Yang, C.; Chen, J. Dual-Strategy of Cation-Doping and Nanoengineering Enables Fast and Stable Sodium-Ion Storage in a Novel Fe/Mn-Based Layered Oxide Cathode. *Adv. Sci.* **2020**, *2002199*. [[CrossRef](#)] [[PubMed](#)]
52. Xiao, Y.; Zhu, Y.-F.; Yao, H.-R.; Wang, P.-F.; Zhang, X.-D.; Li, H.; Yang, X.; Gu, L.; Li, Y.-C.; Wang, T.; et al. A stable layered oxide cathode material for high-performance sodium-ion battery. *Adv. Energy Mater.* **2019**, *9*, 1803978. [[CrossRef](#)]
53. Koo, B.-R.; Sung, K.-W.; Ahn, H.-J. Boosting Ultrafast Lithium Storage Capability of Hierarchical Core/Shell Constructed Carbon Nanofiber/3D Interconnected Hybrid Network with Nanocarbon and FTO Nanoparticle Heterostructures. *Adv. Funct. Mater.* **2020**, *30*, 2001863. [[CrossRef](#)]
54. Yin, H.; Qu, H.-Q.; Liu, Z.; Jiang, R.-Z.; Li, C.; Zhu, M.-Q. Long cycle life and high rate capability of three dimensional  $\text{CoSe}_2$  grainattached carbon nanofibers for flexible sodium-ion batteries. *Nano Energy* **2019**, *58*, 715. [[CrossRef](#)]
55. Liu, J.; Wang, J.; Xu, C.; Jiang, H.; Li, C.; Zhang, L.; Lin, J.; Shen, Z.X. Advanced Energy Storage Devices: Basic Principles, Analytical Methods, and Rational Materials Design. *Adv. Sci.* **2018**, *5*, 1700322. [[CrossRef](#)]
56. Chen, Y.; Guo, J.; Zhuo, Y.; Hu, H.; Liu, W.; Liu, F.; Liu, P.; Yan, J.; Liu, K. An inactive metal supported oxide cathode material with high rate capability for sodium ion batteries. *Energy Storage Mater.* **2019**, *20*, 263. [[CrossRef](#)]
57. Ye, J.; Baumgaertel, A.C.; Wang, Y.M.; Biener, J.; Biener, M.M. Structural Optimization of 3D Porous Electrodes for High-Rate Performance Lithium Ion Batteries. *ACS Nano* **2015**, *9*, 2194. [[CrossRef](#)]
58. Lim, E.; Jo, C.; Kim, H.; Kim, M.-H.; Mun, Y.; Chun, J.; Ye, Y.; Hwang, J.; Ha, K.-S.; Roh, K.C.; et al. Facile Synthesis of  $\text{Nb}_2\text{O}_5$ @Carbon Core-Shell Nanocrystals with Controlled Crystalline Structure for High-Power Anodes in Hybrid Supercapacitors. *ACS Nano* **2015**, *9*, 7497. [[CrossRef](#)]
59. Mao, Y.; Chen, Y.; Qin, J.; Shi, C.; Liu, E.; Zhao, N. Capacitance controlled, hierarchical porous 3D ultra-thin carbon networks reinforced prussian blue for high performance Na-ion battery cathode. *Nano Energy* **2019**, *58*, 192. [[CrossRef](#)]
60. Fang, G.; Wu, Z.; Zhou, J.; Zhu, C.; Cao, X.; Lin, Y.; Chen, Y.; Wang, C.; Pan, A.; Liang, S. Observation of Pseudocapacitive Effect and Fast Ion Diffusion in Bimetallic Sulfides as an Advanced Sodium-Ion Battery Anode. *Adv. Energy Mater.* **2018**, *8*, 1703155. [[CrossRef](#)]
61. Liu, Y.; Liu, X.; Bu, F.; Zhao, X.; Wang, L.; Shen, Q.; Zhang, J.; Zhang, N.; Jiao, L.; Fan, L.-Z. Boosting fast and durable sodium-ion storage by tailoring well-shaped  $\text{Na}_{0.44}\text{MnO}_2$  nanowires cathode. *Electrochim. Acta* **2019**, *313*, 122. [[CrossRef](#)]
62. Wang, Y.; Liu, J.; Lee, B.; Qiao, R.; Yang, Z.; Xu, S.; Yu, X.; Gu, L.; Hu, Y.-S.; Yang, W.; et al. Ti-substituted tunnel-type  $\text{Na}_{0.44}\text{MnO}_2$  oxide as a negative electrode for aqueous sodium-ion batteries. *Nat. Commun.* **2015**, *6*, 6401. [[CrossRef](#)] [[PubMed](#)]
63. Ji, B.; Zhang, F.; Wu, N.; Tang, Y. A Dual-Carbon Battery Based on Potassium-Ion Electrolyte. *Adv. Energy Mater.* **2017**, *7*, 1700920. [[CrossRef](#)]